

# Exogenous delivery of water to Mercury

Kateryna Frantseva<sup>a,b,\*</sup>, David Nesvorný<sup>c</sup>, Michael Mueller<sup>d,e,b</sup>,  
Floris F.S. van der Tak<sup>b,a</sup>, Inge Loes ten Kate<sup>f</sup>, Petr Pokorný<sup>g,h,i</sup>

<sup>a</sup>*Kapteyn Astronomical Institute, University of Groningen, Landleven 12, 9747 AD Groningen, The Netherlands*

<sup>b</sup>*SRON Netherlands Institute for Space Research, Landleven 12, 9747 AD Groningen, The Netherlands*

<sup>c</sup>*Department of Space Studies, Southwest Research Institute, 1050 Walnut Street, Boulder, CO 80302, USA*

<sup>d</sup>*NOVA Netherlands Research School for Astronomy, The Netherlands*

<sup>e</sup>*Leiden Observatory, University of Leiden, Niels Bohrweg 2, 2333 CA Leiden, The Netherlands*

<sup>f</sup>*Department of Earth Sciences, Utrecht University, Budapestlaan 4, 3584 CD Utrecht, The Netherlands*

<sup>g</sup>*Department of Physics, The Catholic University of America, 620 Michigan Ave, NE Washington, DC 20064, USA*

<sup>h</sup>*Astrophysics Science Division, NASA Goddard Space Flight Center, 8800 Greenbelt Rd., Greenbelt, MD 20771, USA*

<sup>i</sup>*Center for Research and Exploration in Space Science and Technology, NASA/GSFC, Greenbelt, MD 20771, USA*

---

## Abstract

Radar and spacecraft observations show the permanently shadowed regions around Mercury's North Pole to contain water ice and complex organic material. One possible source of this material are impacts by interplanetary dust particles (IDPs), asteroids, and comets.

We have performed numerical simulations of the dynamical evolution of asteroids and comets over the few Myr and checked for their impacts with Mercury. We use the N-body integrator RMVS/Swifter to propagate the Sun and the eight planets from their current positions. We add comets and asteroids to the simulations as massless test particles, based on their current orbital distributions. Asteroid impactors are assigned a probability of being water-rich (C-class) based on the measured distribution of taxonomic

---

\*Corresponding author

*Email address:* [frantseva@astro.rug.nl](mailto:frantseva@astro.rug.nl) (Kateryna Frantseva)

types. For comets, we assume a constant water fraction. For IDPs, we use a dynamical meteoroid model to compute the dust flux on Mercury. Relative to previous work on asteroid and comet impacts (Moses et al., 1999), we leverage 20 years of progress in minor body surveys.

Immediate post-impact ejection of impactor material into outer space is taken into account as is the migration efficiency of water across Mercury’s surface to the polar cold traps.

We find that asteroids deliver  $\sim 1 \times 10^3$  kg/yr of water to Mercury, comets deliver  $\sim 1 \times 10^3$  kg/yr and IDPs deliver  $\sim 16 \times 10^3$  kg/yr within a factor of several. Over a timescale of  $\sim 1$  Gyr, this is enough to deliver the minimum amount of water required by the radar and MESSENGER observations.

While other sources of water on Mercury are not ruled out by our analysis, we show that they are not required to explain the currently available observational lower limits.

*Keywords:* Asteroids, dynamics, Comets, dynamics, Interplanetary dust, Mercury, surface, Astrobiology

---

## 1. Introduction

The presence of water in the permanently shadowed polar regions of Mercury is well established. Through ground-based observations of Mercury bright radar-reflective regions were detected near the poles of the planet (Slade et al., 1992; Harmon and Slade, 1992; Butler et al., 1993; Harmon et al., 1994) that are consistent with water ice (although sulphur and certain silicates could also explain the radar data). Based on the radar observations, Moses et al. (1999) determined the total mass of the ice to be  $4 \times 10^{13} - 8 \times 10^{14}$  kg assuming a layer thickness between 2 m and 20 m.

Observations with the Neutron Spectrometer (NS) aboard the MErcury Surface, Space ENvironment, GEochemistry, and Ranging (MESSENGER) spacecraft (Lawrence et al., 2013) demonstrated that the radar-bright deposits in the North polar region consist of water ice. NS was not sensitive to the South polar region due to the eccentric spacecraft orbit. Specifically, NS observations identified a hydrogen-rich layer associated with water ice of unknown thickness, covered by a less hydrogen-rich layer (less than 25 weight % water-equivalent hydrogen) with a thickness between 0.1 and 0.3 m. Lawrence et al. (2013) adopted an ice layer thickness between 0.5 m and 20 m, where the lower limit follows from the models of the surface modi-

fication processes (Crider and Killen, 2005) and the upper limit is estimated from models of radar scattering (Butler et al., 1993).

Additional MESSENGER observations using the Mercury Laser Altimeter (MLA) and the Mercury Dual Imaging System (MDIS) allowed both polar regions to be mapped three-dimensionally, and the area of the permanently shadowed regions to be measured:  $(1.25 - 1.46) \times 10^{10} \text{ m}^2$  around the north pole and  $(4.3 \pm 1.4) \times 10^{10} \text{ m}^2$  around the south pole (Chabot et al., 2012; Neumann et al., 2013).

Combining these two sets of MESSENGER results, and assuming that radar-reflective regions in Mercury’s South polar region are also dominantly water ice with the same layer thickness as in the North, the MESSENGER observations imply a total water mass at Mercury’s poles of  $2.1 \times 10^{13}$  to  $1.4 \times 10^{15} \text{ kg}$  (Lawrence et al., 2013), consistent with the interpretation of ground-based radar observations by Moses et al.. Independently, Eke et al. (2017) derive an upper limit of  $\sim 3 \times 10^{15} \text{ kg}$  from MLA observations of the craters.

Various ideas have been presented as to the origin of Mercury’s water ice. Endogenous sources such as volcanic activity, crust and mantle outgassing, and interaction of surface rocks with the solar wind might have played a role in the formation of the bright and dark deposits on the surface of Mercury (Potter, 1995). Nittler et al. (2017) suggest that Mercury’s polar deposits include some fraction of material derived from volatiles outgassed from Mercury’s interior, potentially caused by volcanic resurfacing (Wilson and Head, 2008; Head et al., 2009; Prockter et al., 2010; Denevi et al., 2013; Ostrach et al., 2015).

On the other hand, water has been delivered from outside of Mercury. In the current Solar System, plausible impactor populations with meaningful water content would be both macroscopic bodies (asteroids and comets) and microscopic impactors (Interplanetary Dust Particles, IDPs). Frantseva et al. (2018) showed that such impacts may be the source of organic material found on the surface of Mars. Could Mercury’s water ice have been deposited in a similar fashion?

Water ice can have accumulated in Mercury’s polar cold traps since the end of the Late Heavy Bombardment  $\sim 3.5 \text{ Gyr}$  ago (Moses et al., 1999) or, equivalently for our purposes, the end of the formation of the terrestrial planets according to the accretion tail scenario (Morbidelli et al., 2018). This idea is reinforced by thermal modeling, demonstrating that the permanently shadowed regions are cold enough to keep water ice thermally stable for

billions of years (Paige et al., 2013). Water ice deposited on other parts of Mercury’s surface is unstable against sublimation; water vapor will diffuse across the surface until it either re-condensates at a polar cold trap or is dissociated by solar ultraviolet radiation and lost to space. Between  $\sim 5 - 15\%$  of the water deposited across Mercury’s surface will reach the polar cold traps (Butler et al., 1993; Butler, 1997); observational evidence for this diffusion process occurring on the surface of the Moon has recently been presented by Hendrix et al. (2019).

Water delivery by impacts of IDPs, asteroids, and comets has been studied in the past, but questions remain. Moses et al. (1999) estimated the water flux due to impacts of asteroids and comets in the last 3.5 Gyr using a Monte Carlo simulation to generate fictitious comets and asteroids, basing themselves on the populations known at the time and (large) correction factors accounting for observational incompleteness. They find that impacts from Jupiter-family comets can supply  $(0.1 - 200) \times 10^{13}$  kg of water to Mercury’s polar regions (corresponding to ice deposits 0.05 – 60 m thick), Halley-type, i.e., long-period comets can supply  $(0.2 - 20) \times 10^{13}$  kg of water to the poles (0.07 – 7 m of ice), and asteroids can provide  $(0.4 - 20) \times 10^{13}$  kg of water to the poles (0.1 – 8 m of ice). In order to calculate the IDP (10 – 500  $\mu\text{m}$ ,) flux on Mercury they extrapolated the current terrestrial influx of IDPs to that at Mercury. The continuous IDP flux on Mercury within the last 3.5 Gyr would deliver  $(3 - 60) \times 10^{13}$  kg of water ice to the permanently shaded regions at Mercury’s poles (equivalent to an average ice thickness of 0.8 – 20 m). More recently, for particles in the size range of 5 – 100  $\mu\text{m}$ , using a numerical code that takes into account the gravitational interaction with all planets and non-gravitational forces such as the Poynting-Robertson drag and the solar wind drag, Borin et al. (2017) have estimated the total impact flux to be  $1.97 \times 10^8$  kg/yr, 20 times higher than the estimate by Moses et al. and 5 times larger than the flux on Earth (Love and Brownlee, 1993). Another study of the dust environment around Mercury has been done by Pokorný et al. (2018) for particles in the size range of 10 – 2000  $\mu\text{m}$ . The total dust flux following from the study is  $4.4 \times 10^6$  kg/yr, similar to Moses et al. and two orders of magnitude less than Borin et al. (2017).

Given the large discrepancy between the existing estimates, and their large uncertainty due to observational incompleteness, we aim to update the asteroid, comet, and dust impact rates on Mercury based on the most recent catalogs of minor bodies, leveraging the results of  $\sim 20$  years of search programs for asteroids and comets since Moses et al. (1999). First, we study

the rates at which comets and asteroids impact Mercury in the current Solar System and we derive the corresponding water delivery rates. We do so using  $N$ -body codes modeling the motions of asteroids and comets under the gravitational influence of the Sun and the planets while checking for impacts. These models are described in Section 2 together with the intrinsic collision probabilities of our asteroid and comet populations and the derived impact rates. Also, we use the ZoDy model from Nesvorný et al. (2010, 2011a,b) to calculate IDP accretion on Mercury in Section 3. In Section 4, we calculate the corresponding water delivery rates on Mercury’s surface. As discussed above, a fraction of the water will be lost to space immediately after impact, as well as during migration to the poles; this fraction is estimated in Section 5. The implications of our findings are discussed in Section 6.

## 2. Gravitational dynamics of asteroids and comets

To study Mercury impact rates in geologically recent times we performed numerical simulations of the gravitational dynamics of the current Solar System. Our model accounts for the gravity of the Sun plus the eight planets Mercury to Neptune. Asteroids and comets are added as different sets of passive test particles, i.e., their gravity is neglected. Non-gravitational forces are also neglected. We integrate forward in time over Myr timescales. Over these timescales, the current Solar System is close to a steady state, even when accounting for the non-gravitational Yarkovsky effect, so we can assume impact rates to be constant with time (see Section 2.1 for a cross-check on this assumption).

To model the gravitational dynamics, we use the  $N$ -body integrator RMVS that corresponds to the RMVS3 version of Swift (Regularized Mixed Variable Symplectic; Levison and Duncan, 1994). The code models the motion of one gravitationally dominant object (Sun) and  $N$  massive objects (in our case:  $N = 8$ ) under the influence of their mutual gravity. Test particles move passively under the influence of the combined gravitational potential of the Sun and the planets. The algorithm handles close approaches by performing a time step regularisation by reducing the time step by a factor of 10 at  $3.5 R_{\text{Hill}}$  and by another factor of 3 at  $1 R_{\text{Hill}}$ .

In order to check for impacts during the simulation the RMVS integrator checks if a test particle and planet are having, or will have within the next time step, an encounter such that the separation distance,  $r$ , is less than some critical radius, the boundary of the encounter region. If this is true

the particle is discarded from the simulation. In order to catch all collisions Swift checks for intersections with planets and switches to an adaptive time step mode. We are confident to set up the “baseline” time step in our models to 1 day in order to well resolve the 88-day orbit of Mercury and those of Mercury crossers.

Test particles are removed from the simulation once they collide with a planet or with the Sun. Moreover, test particles are considered ejected from the Solar System and discarded when they exceed a user-provided heliocentric distance. These values are set separately for asteroid and comet simulations (see Subsections 2.1 and 2.2).

### *2.1. Asteroids*

To model asteroid orbits we have used the MPCORB catalog from February 2017 (epoch K172G). The catalog contains orbital elements for a total of 730,272 asteroids. We culled inaccurate orbits based on single-epoch data, leaving us with 618,078 asteroids to model. We performed our simulations for 10 Myr forward in time in order to get a sufficient number of impactors while avoiding depletion of the impactor orbits. After reaching a heliocentric distance of 1,000 au, asteroids were considered ejected from the Solar System and discarded.

At the end of the simulation 12,480 asteroids were discarded from the system. 6,719 asteroids collided with the Sun, 4,609 asteroids were ejected and 1,152 asteroids collided with the planets. Among the latter, 37 asteroids collided with Mercury, corresponding to an average Mercury impact rate of 3.7 impacts per Myr. In Figure 1, in blue (Simulation 1/K172G) we show the semimajor axes of all 37 impacting asteroids at the start of the simulations. They are distributed between 0.5 au and 3.5 au (Mercury’s semimajor axis is 0.387 au) with a peak near 0.7 au.

As a crosscheck, we have performed two more asteroid simulations using different initial conditions. For the first crosscheck simulation we have used asteroid orbital elements from MPCORB as of July 2016 (epoch K167V, 618,078 asteroids) together with planetary positions for the same date, while for the second crosscheck simulation we have used MPCORB as of March 2018 (epoch K183N, 645,245 asteroids) for the asteroid orbital elements together with the corresponding planetary positions. Both crosscheck simulation samples were cleaned using the same removal condition as for K172G. 43 and 37 asteroids impacted Mercury during the first and second crosscheck simulation, respectively, consistent with our primary result of 37 impactors

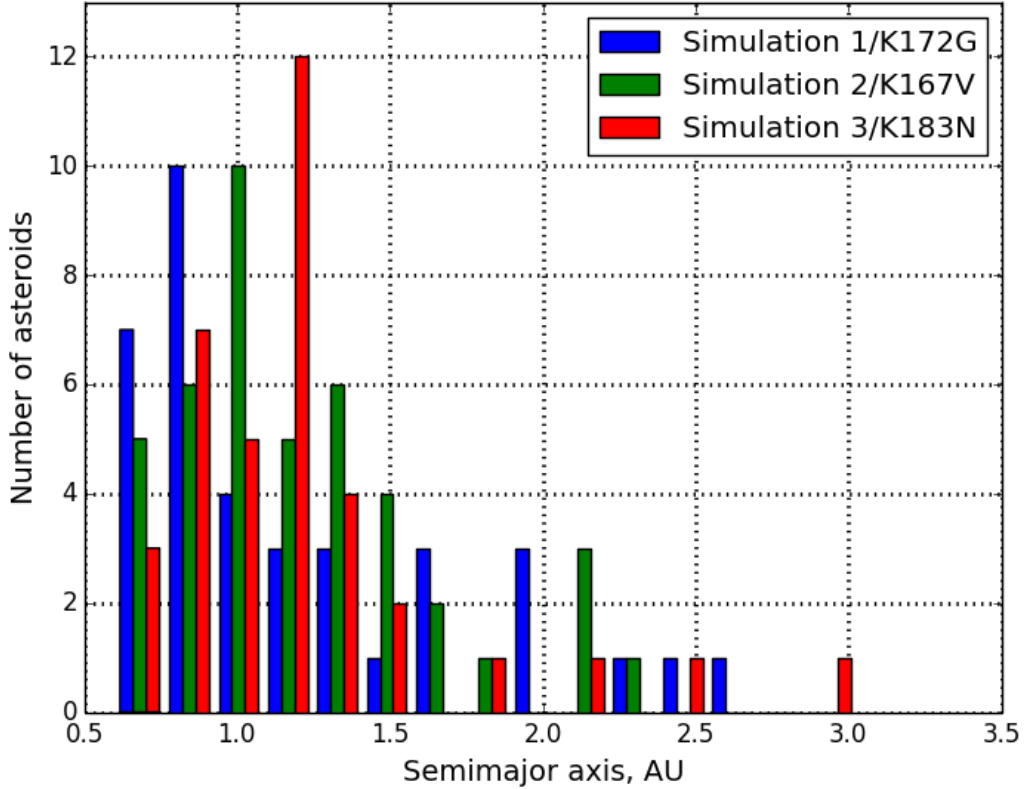


Figure 1: Orbital distribution of the Mercury impacting asteroids. Blue bins correspond to the primary simulation, green bins to the first crosscheck simulation and red bins to the second crosscheck simulation. K172G, K167V and K183N stand for February 2017, July 2016, March 2018, which are the corresponding epochs for each simulation .

within the Poisson noise. The individual asteroids that impact in the first simulation do not impact in the crosscheck simulations and vice versa, which means that our results are valid in a statistical sense, only. We do not identify individual impacts, but we do characterize the population of Mercury impactors.

From here on we will refer to the primary simulation as Simulation 1, to the first crosscheck simulation as Simulation 2 and to the second crosscheck simulation as Simulation 3.

We analyzed the number of asteroids impacting Mercury after each Myr of the simulation as shown in Fig. 2. In this way we studied the time evolution of the Mercury impactors. We expect the number of impactors to

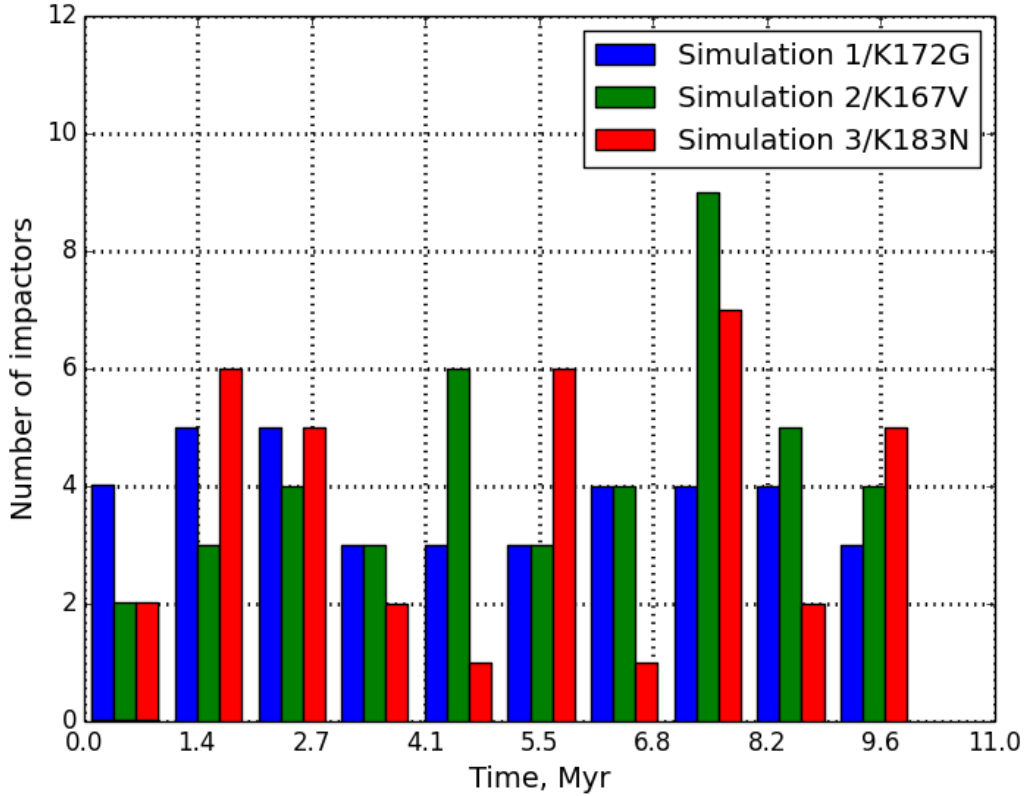


Figure 2: Number of asteroids impacting Mercury per 1 Myr. Blue, green and red colors correspond to the primary and the two crosscheck simulations, respectively.

be proportional to time. Any significant violation of our assumptions (e.g., depletion of asteroids on impactor orbits or Yarkovsky drift) would result in a deviation from this. We did find the total number of impactors to increase steadily, within the  $\sqrt{N}$  Poisson noise, justifying our assumptions.

### 2.1.1. Asteroid collisional probabilities

Apart from recording direct impacts of asteroids in our simulations on Mercury we employ a more statistical approach to estimate the intrinsic collision probabilities of our asteroid populations with Mercury. Every 1 Myr we take the recorded orbital elements of the simulated asteroids ( $a, e, I, \omega$ ) and use two methods to calculate the collision probability of each asteroid with the four terrestrial planets: (1) Kessler (1981) method, and (2) Pokorný and Vokrouhlický (2013) method. These methods calculate the volume of



space swept by the target and the impactor assuming secular evolution of  $(\Omega, \omega)$ , and calculate the collision probability per unit time of two objects of interest. Kessler (1981) requires the  $(a, e, I)$  to be constants and  $(\Omega, \omega)$  to precess uniformly, whereas Pokorný and Vokrouhlický (2013) includes Kozai-Lidov oscillations caused by a single perturbing body on a circular orbit, but requires the target body to be on a coplanar orbit. While neither of these approaches is perfectly reflecting the situation in our simulations, they provide valuable estimates for the asteroid/comet ensemble interaction with Mercury and other terrestrial planets.

For each planet both methods incorporate the effect of gravitational focusing, where the planet’s effective cross-section is

$$\sigma = \pi(r_{\text{pl}} + r_{\text{imp}})^2 \left[ 1 + \frac{V_{\text{esc}}^2}{V_{\text{rel}}^2 + \epsilon^2} \right], \quad (1)$$

where  $r_{\text{pl}}$  is the radius of the target planet,  $r_{\text{imp}}$  is the radius of the impactor,  $V_{\text{esc}}$  is the escape velocity from the target planet,  $V_{\text{rel}}$  is the relative impact velocity between the planet and the target, and  $\epsilon = 0.1 \text{ km s}^{-1}$  is the softening parameter used to avoid singularities for slow impactors. We assume that impactors are much smaller than targets  $r_{\text{pl}} \gg r_{\text{imp}}$ , thus we keep  $r_{\text{imp}} = 0$ .

For each simulated object is at every recorded time step we calculate the collision probability  $\mathcal{P}$  using methods (1) and (2) and then sum  $\mathcal{P}$  for all objects in our simulation which gives us the total collision probability with each planet per unit of time, see Figure 3. Then we multiply the total collision probability with the recording time step (1 Myr) and get the total number of impacts in the recorded time period for methods 1 and 2 resulting in the harmonic mean asteroid impact probability of 4.41 impacts per Myr, which is 19% more than the number of direct impacts.

Note that the Mercury rate is constant/growing, as seen on Figure 3, while the rate decreases with time for Venus, Earth and Mars. The difference in rates is caused by the fact that during the integration the simulated asteroids are injected into regions with the apocenter distance  $Q < 0.90$ , where the asteroids are not currently surveyed very well. Only 10 asteroids with  $Q < 0.9$  are currently known. We do not consider mechanisms that could replenish the currently observed NEO population (i.e. asteroids interacting mainly with Venus, Earth, and Mars in our simulations), but we naturally have a mechanism (close encounters with terrestrial planets), that can inject asteroids into low  $Q$  orbits. In our simulations we start with 4 objects

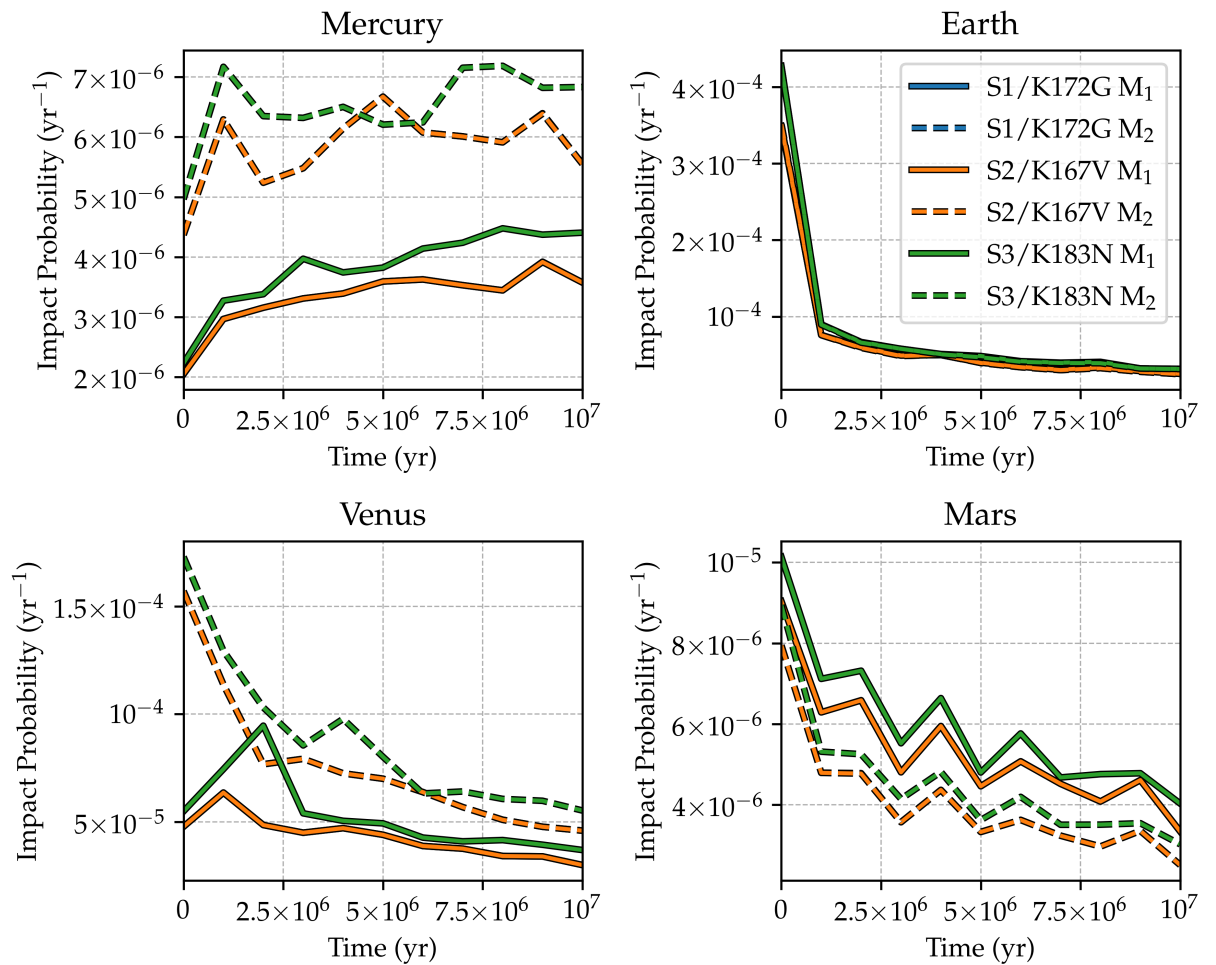


Figure 3: Impact probabilities of asteroids with the four terrestrial planets using (1) Kessler (1981) method (solid lines; M1), and (2) Pokorný and Vokrouhlický (2013) method (dashed lines; M2). Our three simulation epoch color coded: K172G (blue), K167V (orange), K183N (green). Note that K172G and K167V provide almost identical results (< 0.1% difference).

with  $Q < 0.9$  au and after 10 Myr, at the end of the simulations, we have 256 objects with  $Q < 0.9$  au.

## 2.2. Comets

In order to model cometary orbits we have used the MPCORB catalog from November 2016 which contains 893 comets. Of these, we have used 879 comets whose orbits are calculated for the current epoch (removing comets for which the perturbed solutions were absent). As described in Frantseva et al. (2018), the initial cometary set is too small to draw statistically valid conclusions, therefore we have replaced each comet with 5000 synthetic "clone" comets with randomized angular orbital elements (the semimajor axis  $a$ , eccentricity  $e$ , and inclination  $i$  values were kept as of the actual comets). Moreover, Mercury's radius was inflated by a factor of 50. The simulation was performed for 0.1 Myr forward in time; this simulation length was chosen to not significantly deplete the comet population over the course of our simulations. A comet was considered discarded from the simulation if it had collided with a planet, with the Sun, or when it reached a heliocentric distance of 125,000 au. This large threshold value of the heliocentric distance is required by the high eccentricity of some comets.

At the end of the simulation, 76,261 synthetic comets were discarded from the simulation including 3,651 objects that had impacted Mercury. Accounting for cloning of the comets, the inflation of Mercury's radius and the duration of our simulation, this corresponds to  $3,651/5,000/2,500/0.1 = 0.0029$  impacts per Myr.

Like in the case of asteroids, we estimated the uncertainty in our comet result through a crosscheck simulation for a different epoch, November 2017. During the crosscheck simulation 3,684 comets impacted Mercury, consistent with our primary result of 3,651 impactors within the  $\sqrt{N}$  Poisson noise.

### 2.2.1. Steady-state cometary populations and their collisional probabilities

Besides comet simulations based on the MPCORB catalogue, we have also performed comet simulations based on the steady-state models for orbital element distributions for Jupiter Family comets (JFCs), Halley-type comets (HTCs), and Oort cloud Comets (OCCs) as described in Nesvorný et al. (2017) and Vokrouhlický et al. (2019). For the Jupiter Family comets we used the cumulative orbital distributions of ecliptic comets with orbital periods  $P < 20$  yr, Tisserand parameter with respect to Jupiter  $2 < T_J < 3$  and perihelion distance  $q < 2.5$  au as in Figure 7 in Nesvorný et al. (2017).

For the Halley-type comets we used the cumulative orbital distributions with semimajor axes  $10 < a < 20$  au, Tisserand parameter with respect to Jupiter  $T_J < 2$  and perihelion distance  $q < 2$  au as in Figure 11 in Nesvorný et al. (2017). For the Oort cloud comets we have used the cumulative distributions of perihelia and cosine of ecliptic inclination with perihelion distance  $q \leq 5$  au as in Figure 20 in Vokrouhlický et al. (2019). Based on the aforementioned distributions we have generated 10,000 comets for each of the populations and ran simulations similar to the ones performed with the asteroids extracted from MPCORB. The resulting impact probabilities with the four terrestrial planets are shown in Figure 4. Because of their extremely eccentric orbits, OCCs have negligibly small impact probabilities compared to JFCs and HTC. If we take the harmonic mean cometary impact probability of 10,000 synthetic comets (JFCs and HTCs)  $\mathcal{P} = 2.34 \times 10^{-8} \text{ yr}^{-1}$  then we get approximately 0.0021 cometary impacts per Myr assuming the same number of comets (879) as in Sec. 2.2, which is 29% smaller than the number we obtained by simulating the currently known cometary orbits.

### 3. Interplanetary Dust Particles

We use the ZoDy model (Nesvorný et al., 2010, 2011a) to compute the accretion of IDPs on Mercury. In the ZoDy model, IDPs of different sizes are released from asteroids and comets. Their orbital evolution is followed by an efficient  $N$ -body integrator (*Swift*, Levison and Duncan, 1994) until they are ejected from the Solar System, or impact the Sun or a planet. The  $N$ -body integrations include the gravitational effects of the Sun and the planets. Due to the small sizes of the dust particles, non-gravitational forces such as radiation pressure, Poynting-Robertson and solar wind drag are also accounted for. The orbit of each particle is saved at 1,000 yr time intervals, thus allowing us to construct a steady state distribution of orbits for individual sizes. For example, for particles from Jupiter-family comets (JFCs), which probably are the most important source of IDPs in the inner Solar System (see below), we follow the orbital evolution of particles with 28 different sizes from 1  $\mu\text{m}$  to 10 mm. Each set of integrations included 10,000 particles of the same size.

In the absence of mutual collisions between particles, the size distribution of particles in space would be defined by their *initial* size distribution in the source and by their dynamical lifetimes. In the current ZoDy model, the initial size distribution is parametrized by a broken power law with a break

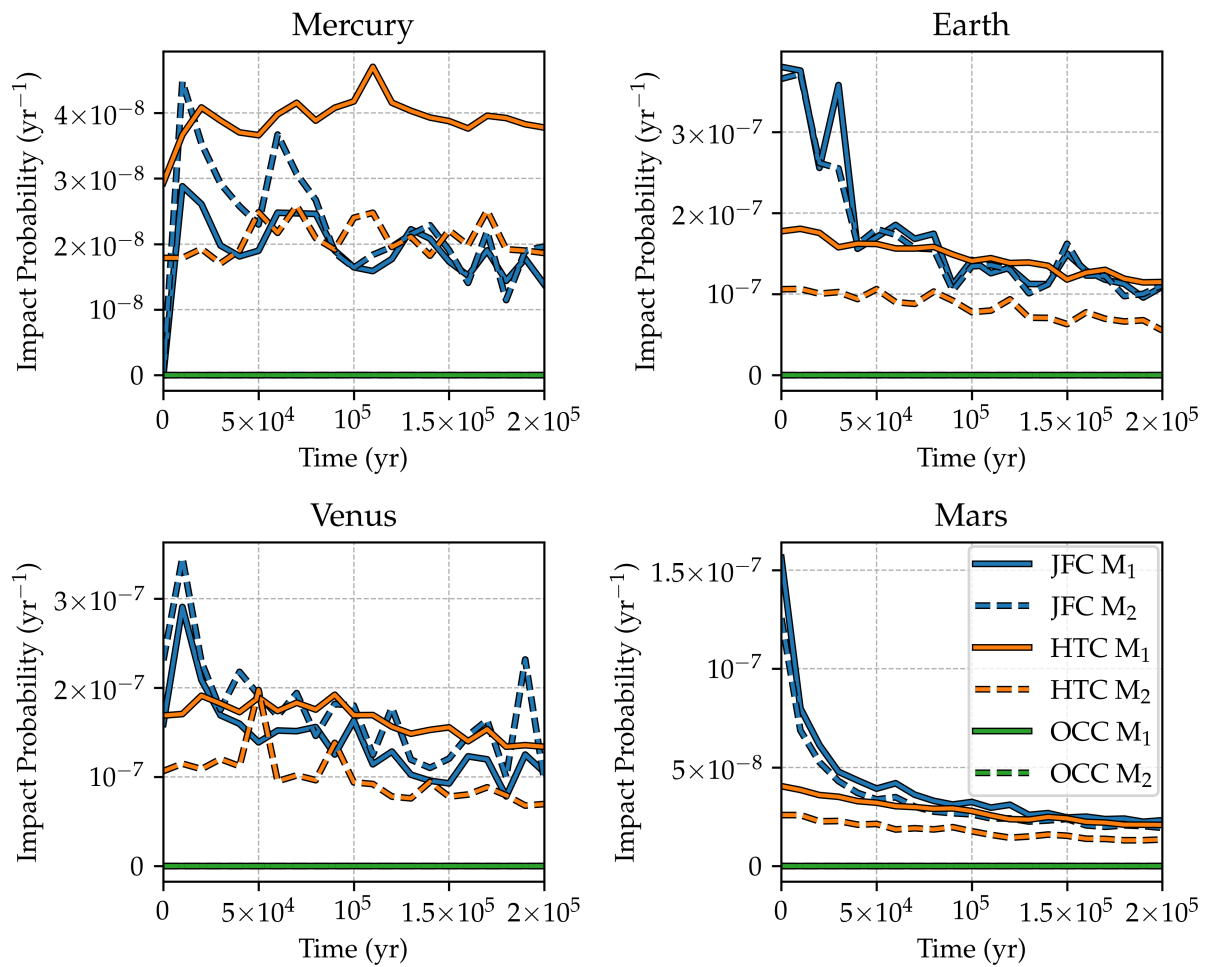


Figure 4: Impact probabilities of JFCs, HTCs and OCCs (10,000 synthetic orbits per population) with the four terrestrial planets using (1) Kessler (1981) method (solid lines; M1), and (2) Pokorný and Vokrouhlický (2013) method (dashed lines; M2). The three cometary populations are color coded: JFCs (blue), HTCs (orange), OCC (green). The OCC flux is 3-5 orders of magnitude smaller than that of JFCs and HTCs.

at diameter  $d^*$ , and differential power law indices  $\gamma_S$  for small particles and  $\gamma_L$  for large particles. Motivated by the comparison of the ZoDy model with the Long Duration Exposure Facility (LDEF) satellite measurements (Love and Brownlee, 1993; Nesvorný et al., 2011a), we use  $d^* \simeq 200 \mu\text{m}$ ,  $\gamma_S \simeq -2$  and  $\gamma_L \simeq -5$ . In this case, both the mass and emission cross-section of IDPs are dominated by  $d \simeq 200 \mu\text{m}$  particles, implying that the mass in micrometeoroids accreted by planets is also dominated by  $d \simeq 200 \mu\text{m}$  particles.

Once the initial size of the particles is fixed, the orbital integrations are used to compute the size distribution of particles at any location in the Solar System. To do this properly, we account for disruptive collisions between particles, which act to destroy parent particles and generate fragments. It is difficult to fully account for the collisional cascade in an  $N$ -body integrator because  $N$  can increase enormously when new particles are added. We therefore adopt a standard approach to this problem (e.g., Grün et al., 1985), where the collisional lifetime,  $\tau_c$ , is defined as a function of size and orbit, and used to decide whether a particle is removed. This approach ignores fragments generated by disruptive collisions. A Poisson random number generator is used to determine whether a particle is disrupted (depending on its size and orbital history).

The orbital dependence of  $\tau_c$  can be determined from first principles (see Nesvorný et al., 2011b, for a discussion). The size dependence, however, is *a priori* unknown and must be treated as a free parameter (or a set of free parameters). In our past work, we used different prescriptions for  $\tau_c(d)$ , including cases from Grün et al. (1985),  $\tau_c(d) = \text{constant}$ , and other dependencies where  $\tau_c$  increases with  $d$ . To fit the meteor data on Earth, for example, we found that  $\tau_c \gtrsim 10^5 \text{ yr}$  for  $d > 100 \mu\text{m}$  (for a reference orbit with  $a = 1 \text{ au}$  and  $e = i = 0$ ).

Nesvorný et al. (2010) used the ZoDy model to determine the relative contribution of asteroid and cometary material to the Zodiacal cloud and the mass in IDPs accreted by the Earth. They found that the mid-infrared (MIR) emission from particles produced in the asteroid belt is mostly confined to within latitudes  $b \lesssim 30^\circ$  of the ecliptic. Conversely, the Zodiacal cloud has a broad latitudinal distribution such that strong thermal emission is observed even in the direction of the ecliptic poles. This shows that asteroidal particles can represent only a small fraction (under 10%, e.g., Carrillo-Sánchez et al., 2016) of the Zodiacal cloud emission. Their contribution to the mass accreted by planets can be larger than that 10%, because asteroid IDPs move on low

eccentricity and low inclination orbits, their velocities with respect to planets are lower, and their impact cross-section is therefore strongly enhanced by gravitational focusing.

Based on a detailed comparison of the dynamical model with MIR observations by the Infrared Astronomical Satellite (IRAS) and the Cosmic Background Explorer (COBE), Nesvorný et al. found that  $\gtrsim 90\%$  of the zodiacal emission at MIR wavelengths comes from dust grains released by JFCs, and only  $\lesssim 10\%$  comes from the long periodic comets. The total mass accreted by the Earth in JFC particles between diameters  $D = 5 \mu\text{m}$  and 1 cm was found to be  $\sim 15 \times 10^6 \text{ kg yr}^{-1}$  (Nesvorný et al. 2011a; factor of 2 uncertainty), which is a large share of the accretion flux measured by LDEF (Love and Brownlee, 1993). Based on these results we consider only IDPs from asteroids and JFCs for our calculations. All other populations, such as long period comets (Wiegert et al., 2009; Pokorný et al., 2014) and the Kuiper belt, are ignored due to their high impact velocities with the Hermean surface ( $> 80 \text{ km/s}$ , Pokorný et al., 2017, 2018) - at these velocities any water content is likely lost to impact vaporization/ionization (e.g., Cintala, 1992). In Section 4.3, we use the ZoDy model for asteroid and JFC particles to determine the impact flux of IDPs on Mercury (also see Pokorný et al., 2018).

#### 4. Water delivery rates

In Sections 2.1 and 2.2, we estimated that Mercury suffers 0.0029 comet impacts per Myr and 3.7 asteroid impacts per Myr. Additionally, our statistical approach yielded 0.0021 cometary impacts per Myr and 4.41 asteroidal impacts per Myr. In this section we will use the direct impact rates and convert them into water delivery rates. Based on the described methods for the IDP flux we will estimate the corresponding water flux on Mercury.

##### 4.1. Asteroids

Asteroids are known to be parent bodies of meteorites. We here focus on the carbonaceous chondrite meteorites, which are known to be water and organic rich. Their water content is  $\sim 10\%$  by mass, their carbon content is  $\sim 2\%$  by mass and their parent bodies are the C type asteroids (National Research Council, 2007; Sephton et al., 2002; Sephton, 2014). By comparison, other taxonomic types contain negligible amounts of water; they are neglected.

To calculate the water delivery rate of the asteroid impacts we use the statistical approach discussed in Frantseva et al. (2018), where each impactor is assigned a probability  $p_C$  of belonging to the C type depending on its semimajor axis at the start of the simulations. The amount of water delivered by an asteroid depends on  $p_C$ , the asteroid mass  $m_{\text{Asteroid}}$  and  $f_{\text{Water}}$ , the water content of carbonaceous chondrite meteorites:

$$M_{\text{Water}} = p_C m_{\text{Asteroid}} f_{\text{Water}}. \quad (2)$$

The water delivery rate equals the sum over all impactors, divided by the duration of our simulation.

The diameter  $D$  of an asteroid is based on the  $H$  magnitude (Bowell et al., 1989) and geometric albedo  $p_V$  (Pravec and Harris, 2007):

$$D = \frac{1329 \text{ km}}{\sqrt{p_V}} 10^{-H/5} \quad (3)$$

where  $p_V = 0.06 \pm 0.01$  (a representative value for C type asteroids, see DeMeo and Carry, 2013, Table 1). Mass follows from diameter adopting an average C type mass density  $\rho$  of  $1.33 \pm 0.58 \text{ g/cm}^3$  (Table 3; Carry, 2012):

$$M = \frac{\pi}{6} D^3 \rho. \quad (4)$$

The probability of an asteroid being part of the C type,  $p_C$ , is estimated based on the initial semimajor axis  $a$  of an asteroid at the start of the simulation. For impactors with  $a < 2 \text{ au}$ , we identify  $p_C$  with the "dark fraction" in the albedo distribution of NEOs as measured by WISE (Wright et al., 2016, dark NEOs are predominantly asteroids of the C class). For the remaining impactors, we use the measured fraction of C types relative to all asteroids derived by DeMeo and Carry (2013), based on NIR spectroscopic surveys. DeMeo and Carry provide two sets of results, before and after debiasing against albedo-dependent survey efficiency, we use the latter. WISE is not subject to such a bias, therefore the C-type fraction for  $a < 2 \text{ au}$  need not be debiased. We adopt  $p_C$  values of 0.253 for  $a < 2 \text{ au}$  (Wright et al., 2016); 0.0612 for  $2 \text{ au} < a < 2.18 \text{ au}$ , the DeMeo and Carry value for  $a = 2.18 \text{ au}$ . For  $a > 2.18 \text{ au}$ , we use C-type fractions specified for each 0.02 au bin in Figure 9 in DeMeo and Carry (2013) (see also Fig. 2 in Frantseva et al., 2018). In practice, the majority of Mercury impactors has  $a < 2 \text{ au}$ , see Fig. 1.



Simulation	Epoch	Number of impactors	Water flux, $10^6$ kg/yr
1	K172G, February 2017	37	$0.021 \pm 0.009$
2	K167V, July 2016	43	$0.023 \pm 0.009$
3	K183N, March 2018	37	$0.430 \pm 0.190$

Table 1: For each of our three asteroid simulations we report the epochs at which they were initialized, the resulting numbers of Mercury impacting asteroids, and the corresponding water fluxes.

Using Equation 2, we estimate a rate of water delivery to Mercury due to asteroid impacts of  $0.021 \pm 0.009 \times 10^6$  kg/yr, averaged over 10 Myr. The uncertainty is calculated combining the known uncertainties of  $H$  magnitude, albedo, and mass density (the uncertainty in  $p_C$  and water content are neglected).

Using the same method, we also analyzed the results of the two cross-check simulations, Simulations 2 and 3, resulting in a mean value for the water delivery rate of  $0.023 \pm 0.009 \times 10^6$  kg/yr and  $0.430 \pm 0.190 \times 10^6$  kg/yr, respectively. While Simulation 2 is in good agreement with Simulation 1, Simulation 3 differs by a factor of nearly 20. We attribute this discrepancy to the different size-distribution of the Mercury impactors: the third simulation contained several relatively big impactors of 2-5 km in diameter, while impactors in the primary and first crosscheck simulation were smaller. The largest few impactors dominate the mass budget, leading to large Poisson noise. Moses et al. (1999) report similar mass-flux differences between simulations due to the mass flux being dominated by the largest few impactors. The results of the three asteroid simulations are listed in Table 1. We adopt the harmonic mean of the three runs,  $0.032 \times 10^6$  kg/yr within a factor of four to five, as our final asteroid delivery rate.

Our calculations are based on the present-day catalogs of asteroids and comets, which are known to be incomplete. They are missing the smallest objects that are too faint to be detected. Nevertheless, the largest asteroids will dominate the total flux while the contribution of the undiscovered asteroids is only  $\sim 4\%$  as described in Frantseva et al. (2018). Observational incompleteness of asteroid catalogs is therefore uncritical for our purposes.

#### 4.2. Comets

The two simulations in Section 2.2 agree on the cometary impactor flux

on Mercury is  $\approx 0.0029$  comets per Myr. In order to calculate a water delivery rate to Mercury we need to know the typical comet mass and water content. We assume the typical comet mass to be  $3 \times 10^{13}$  kg following Swamy (2010). Various comet observations suggests the water content to lay in a range between 3% and 90% (Gicquel et al., 2012; Huebner, 2002; Jewitt, 2004; Taylor et al., 2017) and 50% from the comet nucleus modeling (Priainik, 2002). For our calculations we adopted an average value of 50% due to the diversity of the observed and modeled cometary water content. We estimate the water delivery rate to Mercury to be  $0.044 \times 10^6$  kg/yr.

As in the case of asteroids, our comet catalog is observationally incomplete, with a bias against small, faint objects. We neglect that bias for the same reason as for asteroids. Additionally, we are strongly biased against discovering comets with large orbital periods (due to the finite temporal baseline available). Systematic surveys (aimed at discovering potentially hazardous asteroids, but discovering comets as bycatch) started in the 1990s, so for orbital periods up to 20+ years, our catalogs should be reasonably complete. Those provide the bulk of the water retained on Mercury; longer-period comets hit at very large relative velocity, causing most water to be lost to space (see discussion below). Therefore, observational incompleteness is as uncritical for comets as it is for asteroids.

#### 4.3. Interplanetary Dust Particles

Using the methods described in Section 3, we determine the ratio of IDP impact fluxes between the Earth (here used as a calibration point) and Mercury. For JFC particles, we find that the IDP flux on Earth should be  $\sim 4$  times larger than on Mercury, mainly owing to its larger impact cross-section (the Earth's cross-section is  $\simeq 7$  times larger than that of Mercury). For asteroid particles, the Earth should receive  $\sim 15$  times the IDP accretion of Mercury, a significantly higher ratio than the one obtained for JFC particles. This difference is probably related to stronger gravitational focusing of asteroid IDPs by the Earth (asteroid IDPs have lower inclinations and lower eccentricities, thus lower impact velocities).

We now need to convert these ratios to absolute impact fluxes. For that we use a calibration from Nesvorný et al. (2011a), who found that Earth accretes  $\sim 2 \times 10^7$  kg/yr in JFC IDPs, which is about half of the total input measured by LDEF. If so, Mercury should receive  $5 \times 10^6$  kg/yr of JFC IDPs.

The computation of asteroid IDP flux on Mercury is more uncertain, because we do not have a reliable calibration of asteroid IDP flux on Earth.

For example, if we assume that the asteroid IDPs are responsible for roughly half of the IDP flux measured by LDEF, then we can estimate that Mercury should receive only  $\sim 10^6$  kg/yr in asteroid IDPs (or  $\sim 2 \times 10^6$  kg/yr if asteroid IDPs are responsible for the full flux measured by LDEF). We will adopt  $\sim 10^6$  kg/yr as the asteroid IDP flux to Mercury.

We estimate the joint asteroid and comet IDP flux on Mercury to be  $6 \times 10^6$  kg/yr. Given the uncertainties, our estimate is in good agreement with  $4.4 \times 10^6$  kg/yr by Pokorný et al. (2018), who used a similar model.

Some fraction of IDPs are anhydrous and some are hydrous. The values of these fractions have been studied in the past. It has been estimated that the hydrous IDPs can be from 1% and up to 75% of the total IDPs (Engrand et al., 1999; Noguchi et al., 2002; Dobrica et al., 2010; Zolensky and Lindstrom, 1992). Here we will use  $\sim 40\%$  as a conservative proportion of dust particles initially containing water. The water content of the hydrous dust particles was found to be from 1wt% and up to 40wt% (Engrand et al., 1996). We will use 20% water content of the hydrous dust particles.

All told, we estimate that dust particles deliver  $\sim 0.5 \times 10^6$  kg/yr within a factor of  $\sim 2$  of water to Mercury.

## 5. Water survivability

In the previous section we converted the impact fluxes of asteroids, comets, and IDPs to the corresponding water fluxes. We have shown that Mercury will receive  $0.032 \times 10^6$  kg/yr of water from asteroids,  $0.044 \times 10^6$  kg/yr of water from comets, and  $0.500 \times 10^6$  kg/yr of water from IDPs.

However, only a fraction of this water will be deposited at the poles. A (possibly large) fraction is lost immediately after impact, as impactor material evaporates, forming a supersonic plume, with some of its water content accelerated beyond escape velocity. The water that is retained by Mercury's gravity will migrate across the surface until it is caught at the poles; in the mean-time, some fraction of it is lost to dissociation.

### 5.1. Water loss at impact

Asteroids and comets just like dust particles hit the surface of Mercury at high relative velocity. All impactors including dust particles reach the surface essentially undecelerated by Mercury's tenuous exosphere, not even small dust grains feel Mercury's exosphere appreciably (Ceplecha et al., 1998; Ceplecha and Revelle, 2005). Impacts on planetary surfaces are a topic of

extensive research (see, e.g., Jutzi et al., 2015, for an overview). Impacts cause a (potentially large) fraction of the asteroid, comet and dust material to reach velocities beyond escape velocity immediately after impact, so that material is lost. The fraction of retained impactor material is governed by the relative velocity between impactor and Mercury at the time of impact, the impact speed. Fast impactors will lose most material to space, while material from slower impacts is retained more efficiently. Impact velocity, in turn, depends chiefly on orbital parameters: high  $e$  and high  $i$  favor high impact velocity.

For asteroids and comets we estimate the relative velocity between impactor and Mercury from the RMVS output just before a test particle (asteroid or comet) is discarded, at the time step where the integrator recognizes that the test particle will impact. That time step is much less than one day before the time of impact, and the relative velocity obtained from it should be a good approximation for the actual impact velocity. See Fig. 5 for a histogram of the impact velocities of comets, and Fig. 6 for asteroids. Most of the particles are seen to impact at velocities of 20-40 km/s.

For the interplanetary dust particles we use a distribution of dust mass flux as function of impact velocity from Pokorný et al. (2018, their Figure 22). In particular, we take their mass influx distribution as a function of Mercury’s true anomaly and the impact velocity. We averaged the distribution over Mercury’s orbital period as function of impact velocity and normalise it by the total daily dust flux. Fig. 7 shows the resulting distribution of the total dust flux on Mercury as function of impact velocity.

To estimate the retained mass fraction of asteroids, comets and dust particles upon impact, scaling laws have been established based on comparison between high-speed impact experiments and numerical simulations. We base our analysis on the formalism developed by Svetsov (2011), which is accurate enough for our purposes. To estimate the fraction of the escaped projectile mass,  $\frac{m_p}{m}$ , for the impactors with low impact velocities  $V \leq 15$  km/s, we use their Equation 8:

$$\frac{m_p}{m} = 1 - (0.14 + 0.003V) \ln v_{\text{esc}} - 0.9V^{-0.24}, \quad (5)$$

while for high impact velocities  $V \geq 30$  km/s we use their Equation 9:

$$\frac{m_p}{m} = \exp((0.0015V - 0.2) v_{\text{esc}} + 0.0125V - 0.25), \quad (6)$$

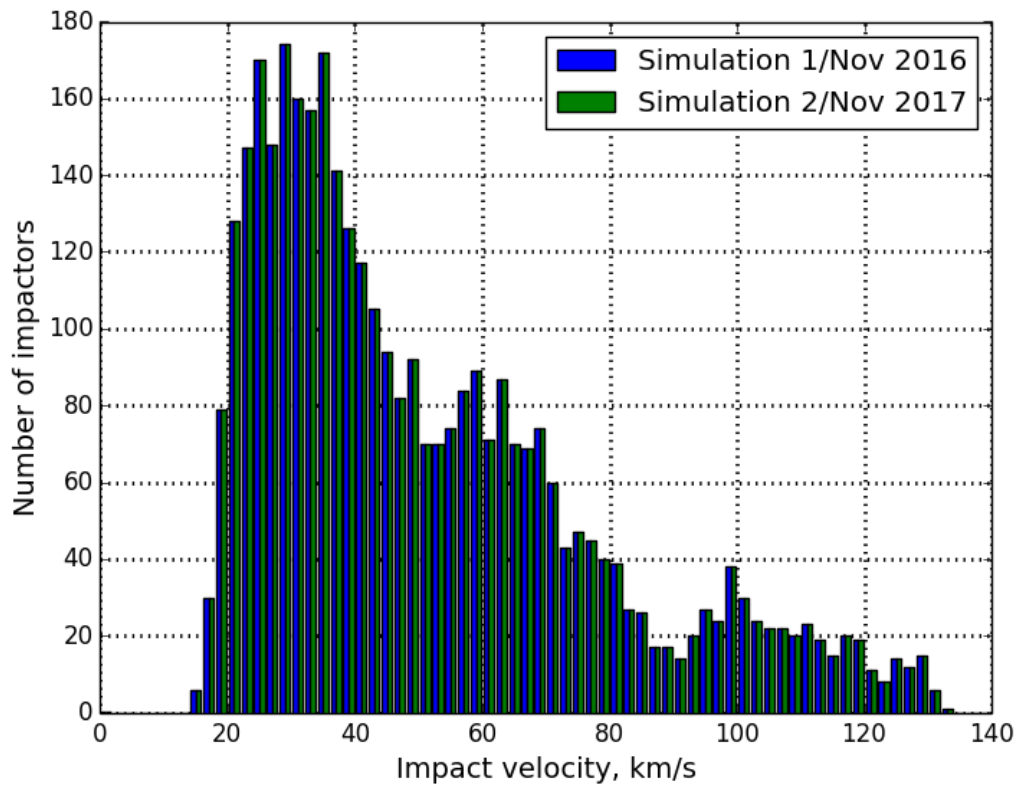


Figure 5: Velocities at which comets impact Mercury. Blue bins correspond to the simulation performed using data from MPCORB as of November 2016 and green bins correspond to the simulation performed using data from MPCORB as of November 2017; the distribution in impact velocity is indistinguishable.

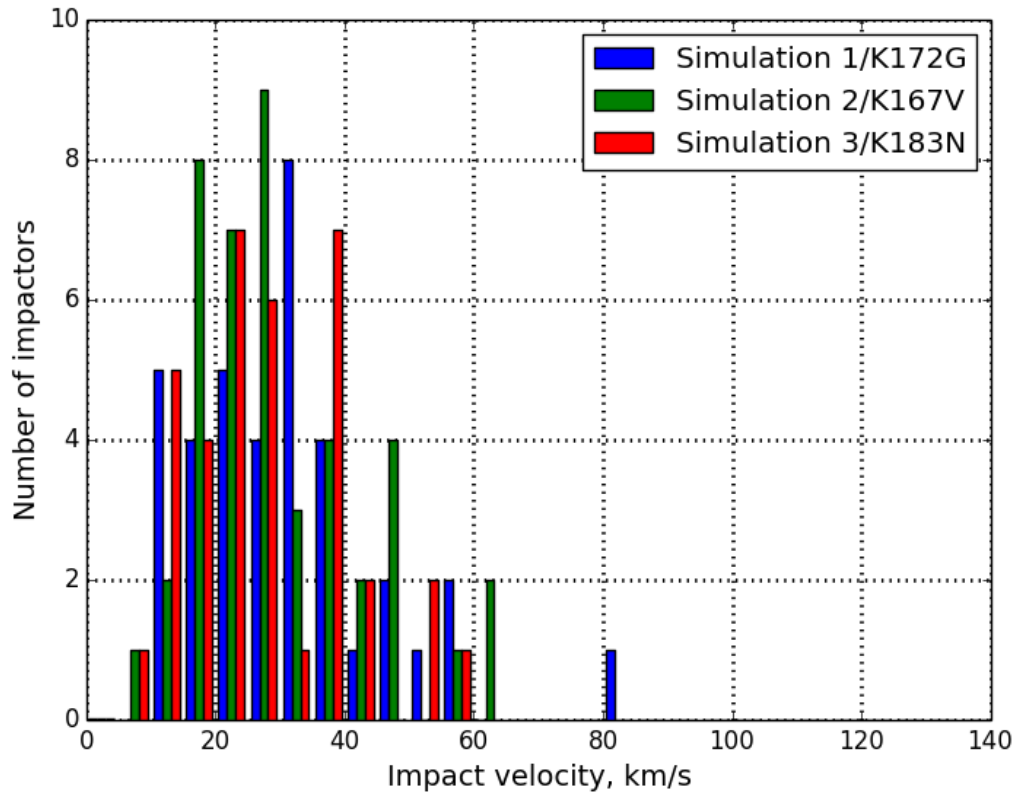


Figure 6: Velocities at which asteroids impact Mercury. Blue bins correspond to the primary simulation, green bins correspond to the first crosscheck simulation and red bins correspond to the second crosscheck simulation.

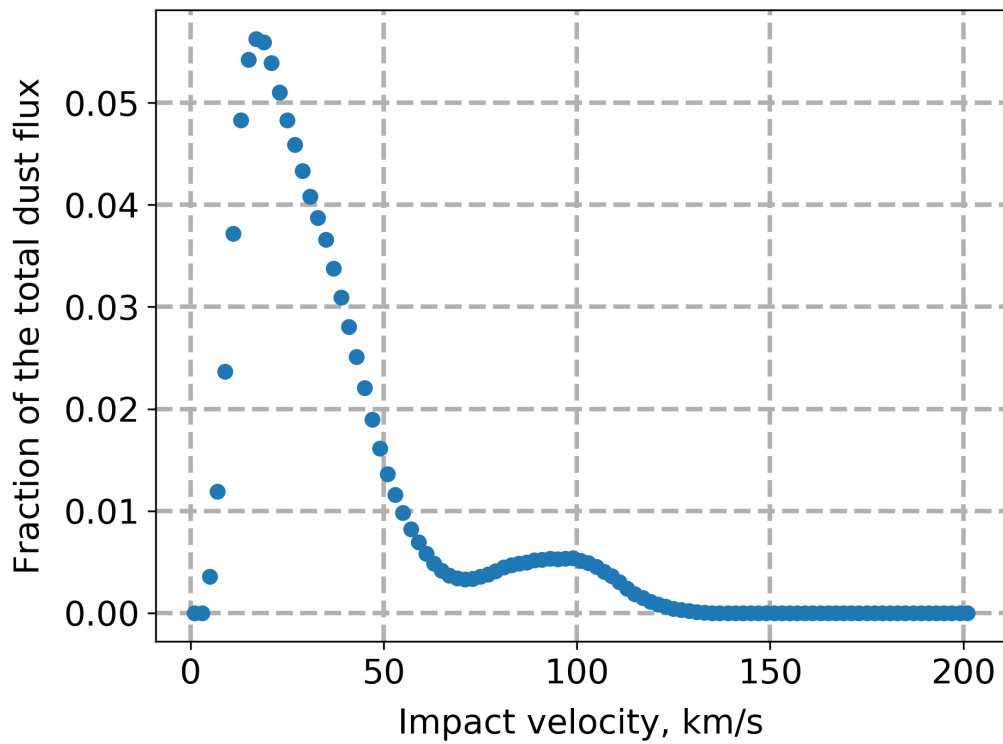


Figure 7: Impact velocity distribution of the total dust flux on Mercury (derived from Pokorný et al., 2018, Figure 22).

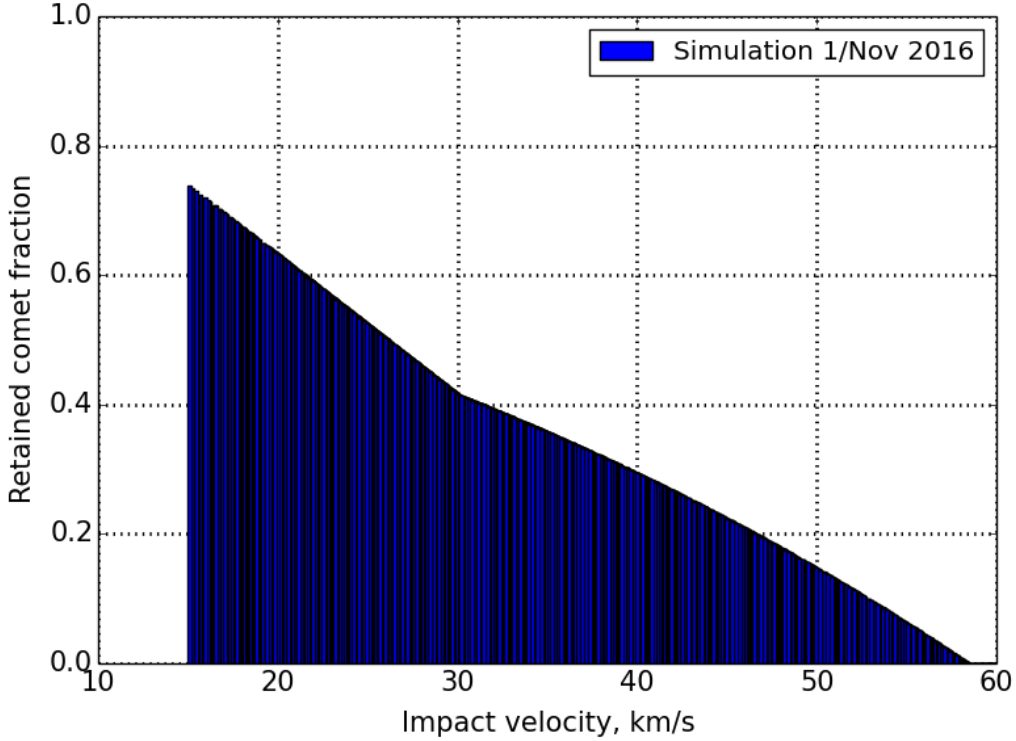


Figure 8: Retained mass fraction of each comet impacting Mercury in the first comet simulation. For impact velocities larger than 60 km/s, all impactor material (and hence all water) is lost to space. The retained mass fraction of the impacting comets in the second simulation is indistinguishable from the first simulation and is not plotted here.

where all velocities are in units of km/s and  $v_{esc} = 4.25$  km/s is Mercury’s escape velocity. In the velocity range between 15 and 30 km/s, we use a linear interpolation between Equations 5 and 6. Figures 8, 9 and 10 illustrate the retained mass fraction,  $1 - \frac{m_p}{m}$ , for each comet and asteroid that impacts Mercury in our simulations and for the total dust flux. For impact velocities up to 45 km/s, at least 20% of material is retained on the surface. For impact velocities beyond 60 km/s, all impactor material is lost to space.

Taking into account the retained fraction of each comet, we estimate the total water flux at Mercury to be  $0.0105 \times 10^6$  kg/yr for the primary comet simulation and  $0.0106 \times 10^6$  kg/yr for the crosscheck comet simulation. Our final adopted cometary retained water flux is  $0.0105 \times 10^6$  kg/yr. For the asteroids, we estimate the water flux at Mercury to be  $0.008 \times 10^6$



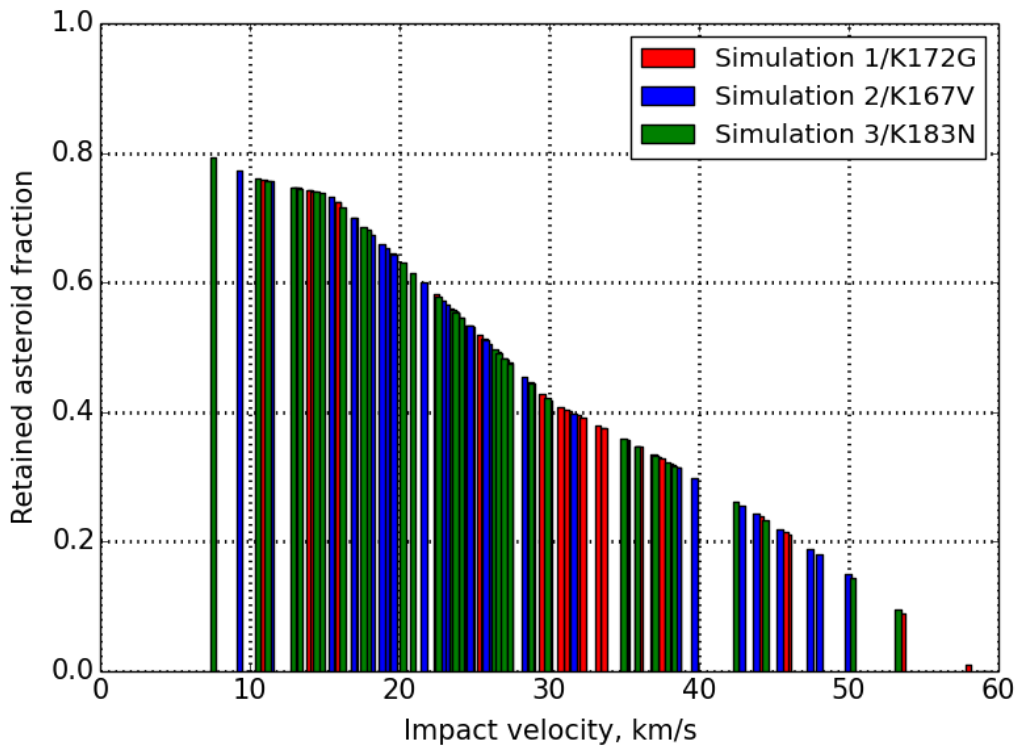


Figure 9: Retained mass fraction of each asteroid impacting Mercury in all three simulations. For impact velocities larger than 60 km/s, all impactor material (and hence all water) is lost to space.

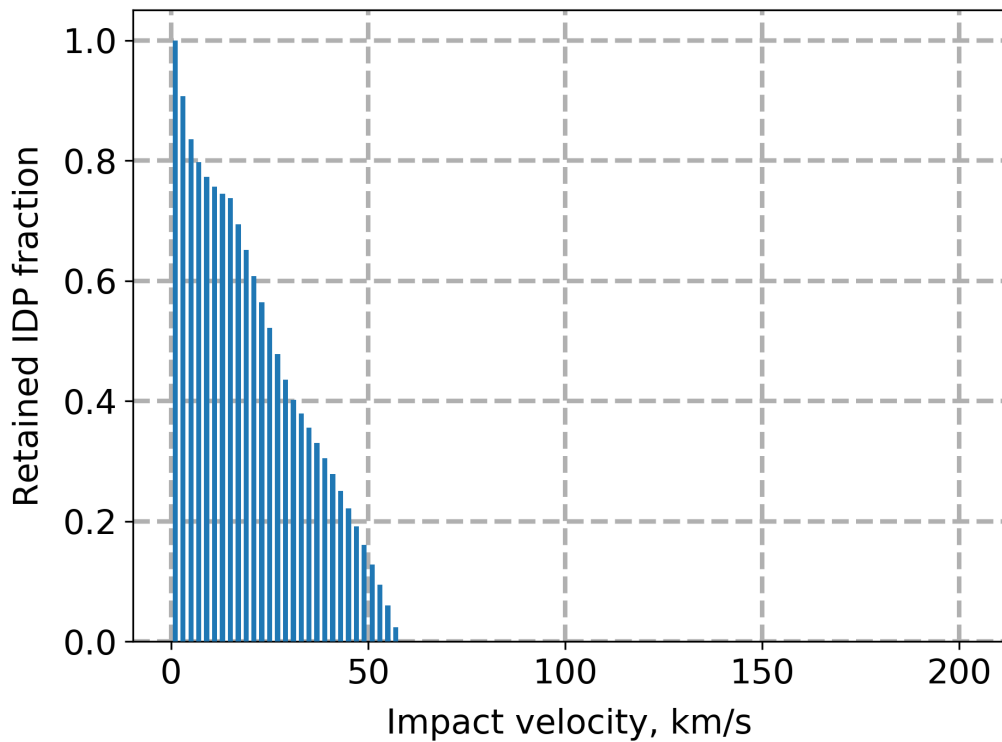


Figure 10: Retained mass fraction of interplanetary dust particles impacting Mercury. For impact velocities larger than 60 km/s, all impactor material (and hence all water) is lost to space.

kg/yr,  $0.013 \times 10^6$  kg/yr and  $0.074 \times 10^6$  kg/yr for the asteroid Simulation 1, Simulation 2, and Simulation 3 correspondingly as shown in Table 2. Our final adopted asteroid retained water flux is the harmonic mean of the range spanned by our results of  $0.014 \times 10^6$  kg/yr within a factor of three. For the interplanetary dust particles, our estimated value of the retained water flux is  $0.207 \times 10^6$  kg/yr.

### 5.2. Water loss during migration to cold traps

Impacts of asteroids, comets and IDPs are spread homogeneously over all latitudes of the planet.<sup>1</sup> Part of the water delivered by the impacts will reach the polar regions through migration processes. Butler et al. (1993); Butler (1997) have performed a Monte Carlo molecule migration simulation to study which fraction of volatiles will be captured in the cold traps of Mercury. Their simulations show that  $\approx 5 - 15\%$  of the water molecules will survive to reach the cold polar regions before being dissociated by solar ultraviolet radiation. Combining the migration rates with our retained water fluxes it follows that  $1 \times 10^3$  kg/yr of asteroid-borne water will be trapped in the permanently shadowed regions, analogously  $1 \times 10^3$  kg/yr of comet-borne water and  $16 \times 10^3$  kg/yr of IDP-borne water. Our final adopted values are the harmonic means of the ranges spanned by our results within a factor of several.

## 6. Discussion

Asteroids, comets, and IDPs are possible exogenous sources of water on Mercury. In the previous sections, we find that asteroids, comets and IDPs deliver  $\sim 1 \times 10^3$  kg/yr,  $\sim 1 \times 10^3$  kg/yr and  $\sim 16 \times 10^3$  kg/yr within a factor of several of water to Mercury’s polar regions, respectively. IDPs are the dominant source of water, while asteroids and comet both deliver about an order of magnitude less.

IDP fluxes on Mercury have also been calculated by Moses et al. (1999), Borin et al. (2017) and Pokorný et al. (2018). Our estimate for the total IDP influx on Mercury,  $6 \times 10^6$  kg/yr, is a factor of 2 lower than the value of Moses

---

<sup>1</sup>Based on MESSENGER observations, Fassett et al. (2012) demonstrated that impact craters on Mercury show a non-uniform distribution in longitude. While we do not attempt to explain that finding, it does not influence our analysis in this section. A hypothetical inhomogeneity in latitude, which is not found, would.

	Incoming flux	Retained flux	Post-migration flux
Simulation 1	$0.021 \pm 0.009 \times 10^6$	$0.008 \times 10^6$	$(0.4 - 1.2) \times 10^3$
Simulation 2	$0.023 \pm 0.009 \times 10^6$	$0.013 \times 10^6$	$(0.7 - 2.0) \times 10^3$
Simulation 3	$0.430 \pm 0.190 \times 10^6$	$0.074 \times 10^6$	$(3.7 - 11.1) \times 10^3$
Final value	$0.032 \times 10^6$	$0.014 \times 10^6$	$1.05 \times 10^3$

Table 2: For each of our three asteroid simulations, we list the corresponding water fluxes before impact (column 1), after post-impact ejection (column 2), and the water flux that successfully migrates to the polar cold traps (column 3). All values are in units of kg/yr. In the last row, we provide our final adopted values of each column, where we adopt the harmonic mean of the ranges spanned by our results; uncertainties are a factor of 4 – 5 in column 1, a factor of  $\sim 3$  in column 2, and a factor of  $\sim 5$  in column 3.

et al. (1999) of  $10^7$  kg/yr, a factor of 40 lower than the value of Borin et al. (2017) of  $2 \times 10^8$  kg/yr and in good agreement with the estimate of  $4.4 \times 10^6$  kg/yr by Pokorný et al. (2018). The difference relative to Moses et al. (1999) can easily be explained by the different adopted values for the measured IDP rate on Earth, reconciling our results. The difference relative to Borin et al. (2017) can be attributed to the fact that our results were calibrated using Love and Brownlee (1993), while Borin et al. (2017) calibrated their results using Cremonese et al. (2012). Also, Borin et al. (2017) do not include mutual meteoroid collisions that are important for Hermean impactors. Thus their model should be treated as the upper limit. As shown in Pokorný et al. (2018) collisions play a major role for all IDPs with diameters  $D > 100 \mu\text{m}$  effectively removing a significant portion of larger asteroidal and JFC meteoroids from the pool of potential Hermean impactors.

Our delivery rates due to asteroid and comet impacts can be compared to the results by Moses et al. (1999). They found that asteroids would deliver  $(0.4 - 20) \times 10^{13}$  kg of ice in 3.5 Gyr, consistent with our estimate of  $\sim 0.4 \times 10^{13}$  kg. Our results should be more accurate than those of Moses et al. (1999), chiefly because they are based on the known distribution of asteroid orbits as of 2018 rather than an extrapolation of the 1994 dataset. Furthermore, our probabilistic approach to define water-rich asteroids is more advanced than the flat 5% water content assumed by Moses et al. (1999).

For comets, Moses et al. (1999) treat Jupiter-family comets and Halley-type comets separately. For the former, they estimate a delivery rate of  $(0.1 - 200) \times 10^{13}$  kg in 3.5 Gyr, and  $(0.2 - 20) \times 10^{13}$  kg in 3.5 Gyr for the latter. Our estimate for water delivered by the entire comet popula-

tion is  $\sim 0.4 \times 10^{13}$  kg in 3.5 Gyr. While these results do agree at the lower range of the quoted uncertainty intervals, much larger delivery rates are allowed by Moses et al. (1999) than by our results. We attribute this chiefly to their large model-dependent correction factors accounting for the observational incompleteness of comets. Compared to them, we benefit from 20 years of systematic sky surveys looking for asteroids (and occasionally discovering comets as bycatch). This should largely eliminate observational incompleteness for large Jupiter-Family Comets with their orbital periods of 20 years or less; correspondingly, we should estimate the delivery rate due to Jupiter-Family Comets rather accurately (note that delivery is dominated by the largest impactors). Delivery due to longer-period comets would be underestimated in our model, on the other hand. However, long-period comets impact at large relative velocities, causing most water to be lost to space. Our comet simulations based on the steady-state models for orbital element distributions for JFCs, HTC, and OCCs (Nesvorný et al., 2017; Vokrouhlický et al., 2019) yielded similar result to the number we obtained by simulating the currently known cometary orbits.

Based on the radar observations the total mass of water ice on Mercury’s poles was calculated to be  $4 \times 10^{13} - 8 \times 10^{14}$  kg (Moses et al., 1999). Using the MESSENGER observations it has been shown that the total mass of water on Mercury’s poles is  $2.1 \times 10^{13}$  to  $1.4 \times 10^{15}$  kg (Lawrence et al., 2013), consistent with the radar result. MESSENGER found the surface area of the permanently shadowed regions around the north pole to be  $(1.25 - 1.46) \times 10^{10}$  m<sup>2</sup> and  $(4.3 \pm 1.4) \times 10^{10}$  m<sup>2</sup> around the south pole. Combining the neutron and radar data from the MESSENGER spacecraft, the water ice origin of the radar-reflective deposits was confirmed for the North polar region (NS was not sensitive to the South due to the spacecraft’s eccentric orbit). The total amount of water in the deposits is calculated based on the assumption that the South pole deposits have the same composition (Lawrence et al., 2013). Additionally, estimates of the deposit mass, based on MESSENGER observations, assume that the deposits are between 0.5 m and 20 m deep. That layer depth follows from models of surface modification processes (Crider and Killen, 2005) and from models of the radar scattering (Butler et al., 1993), not from MESSENGER data directly.

We find that impacts of IDPs, asteroids, and comets deliver  $\sim 18 \times 10^3$  kg/yr of water to Mercury’s poles. This is easily enough to explain the observational lower limit on the ice-layer thickness of  $2.1 \times 10^{13}$  kg; delivery would take  $\sim 1$  Gyr. While our analysis does not rule out any other sources

of water ice on Mercury, we do show that none are needed to explain the (lower limits on the) data available today. Over 3.5 Gyr impacts of dust, asteroids and comets would deliver up to  $6 \times 10^{13}$  kg. More is allowed but not required by the data. Should evidence for more water ice than  $6 \times 10^{13}$  kg be found in the future, this would necessitate additional water sources beyond impacts.

When converting the number of asteroid impacts to the water flux we focused on the C type asteroids parent bodies of chondrite meteorites, assuming their water content to be  $\sim 10\%$  by mass (National Research Council, 2007; Sephton et al., 2002; Sephton, 2014). Recent study by Rivkin and DeMeo (2019) shows that C-type asteroids appear to have a significantly lower water content than chondrite meteorites. They argue that only a certain fraction, around 40% of C type asteroids should be considered water rich. If the above-mentioned values have been adopted in this paper, it would bring the asteroid delivered water flux to Mercury down by 40%.

IDPs, comets, and C-type asteroids are not only rich in water but also in organic molecules. While an endogenous contribution to Mercury's water cannot be ruled out, there is no plausible endogenous formation mechanism for organics; therefore any positive detection of organics would prove the exogenous origin of the bright and dark deposits (Zhang and Paige, 2009).

For a better understanding of the nature and the origin of the dark and bright deposits in the polar regions of Mercury, more observational data are needed. For example, investigating various isotopic ratios, like D/H and  $^{14}\text{N}/^{15}\text{N}$  for the Earth, may be a way to constrain the origins of Mercury's water. The joint ESA-JAXA mission BepiColombo, launched in 2018 and scheduled to arrive at Mercury in 2025, will guide further exploration. BepiColombo's polar orbit will be much less eccentric than that of MESSENGER. This will allow to perform elemental measurements of the southern hemisphere that were made with poor spatial resolution or even not possible before. Importantly for our purposes, BepiColombo carries the Mercury Gamma-Ray and Neutron Spectrometer (MGNS), similar to MESSENGER's NS but at higher resolution. MGNS will map water across the entire surface of Mercury, including the Southern polar regions, down to a depth of 1–2 m (Mitrofanov et al., 2010) and will clarify if the Southern polar region is indeed as water-rich as its Northern counterpart.

## 7. Conclusions

IDPs, asteroids and comets play an important role in the formation process of the dark and bright deposits in the polar regions of Mercury that have been associated with water ice. While other sources are not ruled out by our analysis, we show that impacts can deliver a sufficient amount of water to Mercury's polar regions to explain the available observational data; delivery would take  $\sim 1$  Gyr. IDPs deliver more water than asteroids and comets combined.

## 8. Acknowledgments

This paper is dedicated to the brave resistance of Ukrainian people.

We are thankful to *David E. Kaufmann* for valuable help with RMVS/Swifter, *Cecile Engrand* and *Mikhail Zelensky* for input on the water fraction of IDPs. This research has made use of data and/or services provided by the International Astronomical Union's Minor Planet Center. We would like to thank the Center for Information Technology of the University of Groningen for their support and for providing access to the Peregrine high performance computing cluster. Petr Pokorný's work was supported by NASA awards number 80GSFC21M0002 and 80NSSC21K0153. The authors thank the two anonymous reviewers for their thoughtful comments, which significantly improved the manuscript.

## References

- Borin, P., Cremonese, G., Marzari, F., Lucchetti, A., 2017. Asteroidal and cometary dust flux in the inner solar system. *A&A* .
- Bowell, E., Hapke, B., Domingue, D., Lumme, K., Peltoniemi, J., Harris, A. W., 1989. Application of photometric models to asteroids. In: Binzel, R. P., Gehrels, T., Matthews, M. S. (Eds.), *Asteroids II*. pp. 524–556.
- Butler, B. J., Aug. 1997. The migration of volatiles on the surfaces of Mercury and the Moon. *J. Geophys. Res.* 102, 19283–19292.
- Butler, B. J., Muhleman, D. O., Slade, M. A., Aug. 1993. Mercury - Full-disk radar images and the detection and stability of ice at the North Pole. *J. Geophys. Res.* 98, 15.

- Carrillo-Sánchez, J. D., Nesvorný, D., Pokorný, P., Janches, D., Plane, J. M. C., Dec. 2016. Sources of cosmic dust in the Earth's atmosphere. *Geophys. Res. Lett.* 43, 11.
- Carry, B., Dec. 2012. Density of asteroids. *Planet. Space Sci.* 73, 98–118.
- Ceplecha, Z., Borovička, J., Elford, W. G., Revelle, D. O., Hawkes, R. L., Porubčan, V., Šimek, M., Sep 1998. Meteor Phenomena and Bodies. *Space Sci. Rev.* 84, 327–471.
- Ceplecha, Z., Revelle, D. O., Jan 2005. Fragmentation model of meteoroid motion, mass loss, and radiation in the atmosphere. *Meteoritics and Planetary Science* 40, 35.
- Chabot, N. L., Ernst, C. M., Denevi, B. W., Harmon, J. K., Murchie, S. L., Blewett, D. T., Solomon, S. C., Zhong, E. D., May 2012. Areas of permanent shadow in Mercury's south polar region ascertained by MESSENGER orbital imaging. *Geophys. Res. Lett.* 39, L09204.
- Cintala, M. J., Jan. 1992. Impact-induced thermal effects in the lunar and mercurian regoliths. *J. Geophys. Res.* 97 (E1), 947–973.
- Cremonese, G., Borin, P., Martellato, E., Marzari, F., Bruno, M., Apr 2012. New Calibration of the Micrometeoroid Flux on Earth. *ApJ* 749 (2), L40.
- Crider, D., Killen, R. M., Jun. 2005. Burial rate of Mercury's polar volatile deposits. *Geophys. Res. Lett.* 32, L12201.
- DeMeo, F. E., Carry, B., Sep. 2013. The taxonomic distribution of asteroids from multi-filter all-sky photometric surveys. *Icarus* 226, 723–741.
- Denevi, B. W., Ernst, C. M., Meyer, H. M., Robinson, M. S., Murchie, S. L., Whitten, J. L., Head, J. W., Watters, T. R., Solomon, S. C., Ostrach, L. R., Chapman, C. R., Byrne, P. K., Klimczak, C., Peplowski, P. N., May 2013. The distribution and origin of smooth plains on Mercury. *Journal of Geophysical Research (Planets)* 118 (5), 891–907.
- Dobrica, E., Engrand, C., Duprat, J., Gounelle, M., Sep. 2010. A Statistical Overview of CONCORDIA Antarctic Micrometeorites. *Meteoritics and Planetary Science Supplement* 73, 5213.



- Eke, V. R., Lawrence, D. J., Teodoro, L. F. A., Mar. 2017. How thick are Mercury's polar water ice deposits? *Icarus* 284, 407–415.
- Engrand, C., Deloule, E., Hoppe, P., Kurat, G., Maurette, M., Robert, F., Mar. 1996. Water Contents of Micrometeorites from Antarctica. In: Lunar and Planetary Science Conference. Vol. 27 of Lunar and Planetary Science Conference.
- Engrand, C., Deloule, E., Robert, F., Maurette, M., Kurat, G., Sep. 1999. Extraterrestrial water in micrometeorites and cosmic spherules from Antarctica: an ion microprobe study. *Meteoritics and Planetary Science* 34, 773–786.
- Fassett, C. I., Head, J. W., Baker, D. M. H., Zuber, M. T., Smith, D. E., Neumann, G. A., Solomon, S. C., Klimczak, C., Strom, R. G., Chapman, C. R., Prockter, L. M., Phillips, R. J., Oberst, J., Preusker, F., Oct. 2012. Large impact basins on Mercury: Global distribution, characteristics, and modification history from MESSENGER orbital data. *Journal of Geophysical Research (Planets)* 117, E00L08.
- Frantseva, K., Mueller, M., ten Kate, I. L., van der Tak, F. F. S., Greenstreet, S., Jul. 2018. Delivery of organics to Mars through asteroid and comet impacts. *Icarus* 309, 125–133.
- Gicquel, A., Bockelée-Morvan, D., Zakharov, V. V., Kelley, M. S., Woodward, C. E., Wooden, D. H., Jun. 2012. Investigation of dust and water ice in comet 9P/Tempel 1 from Spitzer observations of the Deep Impact event. *A&A* 542, A119.
- Grun, E., Zook, H. A., Fechtig, H., Giese, R. H., May 1985. Collisional balance of the meteoritic complex. *Icarus* 62, 244–272.
- Harmon, J. K., Slade, M. A., Oct. 1992. Radar mapping of Mercury - Full-disk images and polar anomalies. *Science* 258, 640–643.
- Harmon, J. K., Slade, M. A., Vélez, R. A., Crespo, A., Dryer, M. J., Johnson, J. M., May 1994. Radar mapping of Mercury's polar anomalies. *Nature* 369, 213–215.
- Head, J. W., Murchie, S. L., Prockter, L. M., Solomon, S. C., Chapman, C. R., Strom, R. G., Watters, T. R., Blewett, D. T., Gillis-Davis, J. J.,

- Fassett, C. I., Dickson, J. L., Morgan, G. A., Kerber, L., Aug 2009. Volcanism on Mercury: Evidence from the first MESSENGER flyby for extrusive and explosive activity and the volcanic origin of plains. *Earth and Planetary Science Letters* 285 (3-4), 227–242.
- Hendrix, A. R., Hurley, D. M., Farrell, W. M., Greenhagen, B. T., Hayne, P. O., Retherford, K. D., Vilas, F., Cahill, J. T. S., Poston, M. J., Liu, Y., 2019. Diurnally-migrating lunar water: Evidence from ultraviolet data. *Geophysical Research Letters* 46, 2417–2424.  
URL <https://agupubs.onlinelibrary.wiley.com/doi/abs/10.1029/2018GL081821>
- Huebner, W. F., Oct. 2002. Composition of Comets: Observations and Models. *Earth Moon and Planets* 89, 179–195.
- Jewitt, D. C., 2004. From cradle to grave: the rise and demise of the comets. pp. 659–676.
- Jutzi, M., Holsapple, K., Wünneman, K., Michel, P., Feb. 2015. Modeling asteroid collisions and impact processes. ArXiv e-prints.
- Kessler, D. J., Oct. 1981. Derivation of the collision probability between orbiting objects: the lifetimes of jupiter’s outer moons. *Icarus* 48 (1), 39–48.
- Lawrence, D. J., Feldman, W. C., Goldsten, J. O., Maurice, S., Peplowski, P. N., Anderson, B. J., Bazell, D., McNutt, R. L., Nittler, L. R., Prettyman, T. H., Rodgers, D. J., Solomon, S. C., Weider, S. Z., Jan. 2013. Evidence for Water Ice Near Mercury’s North Pole from MESSENGER Neutron Spectrometer Measurements. *Science* 339, 292.
- Levison, H. F., Duncan, M. J., Mar. 1994. The long-term dynamical behavior of short-period comets. *Icarus* 108, 18–36.
- Love, S. G., Brownlee, D. E., Oct. 1993. A Direct Measurement of the Terrestrial Mass Accretion Rate of Cosmic Dust. *Science* 262, 550–553.
- Mitrofanov, I. G., Kozyrev, A. S., Konovalov, A., Litvak, M. L., Malakhov, A. A., Mokrousov, M. I., Sanin, A. B., Tret’ukov, V. I., Vostrukhin, A. V., Bobrovnikskij, Y. I., Tomilina, T. M., Gurvits, L., Owens, A., Jan. 2010. The Mercury Gamma and Neutron Spectrometer (MGNS) on board the

- Planetary Orbiter of the BepiColombo mission. *Planet. Space Sci.* 58, 116–124.
- Morbidelli, A., Nesvorný, D., Laurenz, V., Marchi, S., Rubie, D. C., Elkins-Tanton, L., Wieczorek, M., Jacobson, S., May 2018. The timeline of the lunar bombardment: Revisited. *Icarus* 305, 262–276.
- Moses, J. I., Rawlins, K., Zahnle, K., Dones, L., Feb. 1999. External Sources of Water for Mercury’s Putative Ice Deposits. *Icarus* 137, 197–221.
- National Research Council, 2007. Exploring Organic Environments in the Solar System.
- Nesvorný, D., Janches, D., Vokrouhlický, D., Pokorný, P., Bottke, W. F., Jenniskens, P., Dec. 2011a. Dynamical Model for the Zodiacal Cloud and Sporadic Meteors. *ApJ* 743, 129.
- Nesvorný, D., Jenniskens, P., Levison, H. F., Bottke, W. F., Vokrouhlický, D., Gounelle, M., Apr. 2010. Cometary Origin of the Zodiacal Cloud and Carbonaceous Micrometeorites. Implications for Hot Debris Disks. *ApJ* 713, 816–836.
- Nesvorný, D., Vokrouhlický, D., Dones, L., Levison, H. F., Kaib, N., Morbidelli, A., Aug. 2017. Origin and Evolution of Short-period Comets. *ApJ* 845 (1), 27.
- Nesvorný, D., Vokrouhlický, D., Pokorný, P., Janches, D., Dec. 2011b. Dynamics of Dust Particles Released from Oort Cloud Comets and Their Contribution to Radar Meteors. *ApJ* 743, 37.
- Neumann, G. A., Cavanaugh, J. F., Sun, X., Mazarico, E. M., Smith, D. E., Zuber, M. T., Mao, D., Paige, D. A., Solomon, S. C., Ernst, C. M., Barnouin, O. S., Jan. 2013. Bright and Dark Polar Deposits on Mercury: Evidence for Surface Volatiles. *Science* 339, 296.
- Nittler, L. R., Chabot, N. L., Grove, T. L., Peplowski, P. N., Dec 2017. The Chemical Composition of Mercury. arXiv e-prints, arXiv:1712.02187.
- Noguchi, T., Nakamura, T., Nozaki, W., Sep. 2002. Mineralogy of phyllosilicate-rich micrometeorites and comparison with Tagish Lake and Sayama meteorites. *Earth and Planetary Science Letters* 202, 229–246.

- Ostrach, L. R., Robinson, M. S., Whitten, J. L., Fassett, C. I., Strom, R. G., Head, J. W., Solomon, S. C., Apr 2015. Extent, age, and resurfacing history of the northern smooth plains on Mercury from MESSENGER observations. *Icarus* 250, 602–622.
- Paige, D. A., Siegler, M. A., Harmon, J. K., Neumann, G. A., Mazarico, E. M., Smith, D. E., Zuber, M. T., Harju, E., Delitsky, M. L., Solomon, S. C., Jan. 2013. Thermal Stability of Volatiles in the North Polar Region of Mercury. *Science* 339, 300.
- Pokorný, P., Sarantos, M., Janches, D., Jun. 2017. Reconciling the Dawn–Dusk Asymmetry in Mercury’s Exosphere with the Micrometeoroid Impact Directionality. *ApJ* 842, L17.
- Pokorný, P., Sarantos, M., Janches, D., Aug. 2018. A Comprehensive Model of the Meteoroid Environment around Mercury. *ApJ* 863, 31.
- Pokorný, P., Vokrouhlický, D., Sep. 2013. Öpik-type collision probability for high-inclination orbits: Targets on eccentric orbits. *Icarus* 226 (1), 682–693.
- Pokorný, P., Vokrouhlický, D., Nesvorný, D., Campbell-Brown, M., Brown, P., Jul. 2014. Dynamical Model for the Toroidal Sporadic Meteors. *ApJ* 789 (1), 25.
- Potter, A. E., 1995. Chemical sputtering could produce sodium vapor and ice on Mercury. *Geophys. Res. Lett.* 22, 3289–3292.
- Pravec, P., Harris, A. W., Sep. 2007. Binary asteroid population. 1. Angular momentum content. *Icarus* 190, 250–259.
- Prialnik, D., Oct. 2002. Modeling the Comet Nucleus Interior. *Earth Moon and Planets* 89, 27–52.
- Prockter, L. M., Ernst, C. M., Denevi, B. W., Chapman, C. R., Head, J. W., Fassett, C. I., Merline, W. J., Solomon, S. C., Watters, T. R., Strom, R. G., Cremonese, G., Marchi, S., Massironi, M., Aug 2010. Evidence for Young Volcanism on Mercury from the Third MESSENGER Flyby. *Science* 329 (5992), 668.

- Rivkin, A. S., DeMeo, F. E., Jan. 2019. How Many Hydrated NEOs Are There? *Journal of Geophysical Research (Planets)* 124 (1), 128–142.
- Sephton, M. A., Oct. 2014. *Organic Geochemistry of Meteorites*.
- Sephton, M. A., Wright, I. P., Gilmour, I., de Leeuw, J. W., Grady, M. M., Pillinger, C. T., Jun. 2002. High molecular weight organic matter in martian meteorites. *Planetary and Space Sciences Research Institute* 50, 711–716.
- Slade, M. A., Butler, B. J., Muhleman, D. O., Oct. 1992. Mercury radar imaging - Evidence for polar ice. *Science* 258, 635–640.
- Svetsov, V., Jul. 2011. Cratering erosion of planetary embryos. *Icarus* 214, 316–326.
- Swamy, K. S. K., 2010. *Physics of Comets (3rd Edition)*. World Scientific Publishing Co.
- Taylor, M. G. G. T., Altobelli, N., Buratti, B. J., Choukroun, M., May 2017. The Rosetta mission orbiter science overview: the comet phase. *Philosophical Transactions of the Royal Society of London Series A* 375, 20160262.
- Vokrouhlický, D., Nesvorný, D., Dones, L., May 2019. Origin and Evolution of Long-period Comets. *AJ* 157 (5), 181.
- Wiegert, P., Vaubaillon, J., Campbell-Brown, M., May 2009. A dynamical model of the sporadic meteoroid complex. *Icarus* 201 (1), 295–310.
- Wilson, L., Head, J. W., Dec 2008. Volcanism on Mercury: A new model for the history of magma ascent and eruption. *Geophys. Res. Lett.* 35 (23), L23205.
- Wright, E. L., Mainzer, A., Masiero, J., Grav, T., Bauer, J., Oct. 2016. The Albedo Distribution of Near Earth Asteroids. *AJ* 152, 79.
- Zhang, J. A., Paige, D. A., Aug. 2009. Cold-trapped organic compounds at the poles of the Moon and Mercury: Implications for origins. *Geophys. Res. Lett.* 36, L16203.

Zolensky, M. E., Lindstrom, D. J., 1992. Mineralogy of 12 large 'chondritic' interplanetary dust particles. In: Ryder, G., Sharpton, V. L. (Eds.), Lunar and Planetary Science Conference Proceedings. Vol. 22 of Lunar and Planetary Science Conference Proceedings. pp. 161–169.